A fully nonlinear potential flow wave modelling procedure for simulations of offshore sea states with various wave breaking scenarios

Weizhi Wang *[1], Csaba Pákozdi[2], Arun Kamath[1], and Hans Bihs[1]

[1]Department of Civil and Environmental Engineering, Norwegian University of Science and Technology (NTNU), 7491 Trondheim, Norway
[2]SINTEF Ocean, Otto Nielsens veg 10, 7052 Trondheim, Norway

Applied Ocean Research, 2021, **117**, pp. 102898.
DOI: http://dx.doi.org/10.1016/j.apor.2021.102898

Abstract

An accurate representation of a given sea state is crucial for the study of hydrodynamic loads on offshore structures. It is straightforward to check the quality of the reproduced regular waves in a numerical wave tank (NWT). However, many more parameters need to be considered to ensure the quality of irregular waves. In this paper, a fully non-linear potential flow (FNPF) wave model is used to reproduce irregular sea states with different severity of wave breaking. The numerical model solves the velocity potential from the Laplace equation and the free surface boundary conditions using a finite difference method on a σ-coordinate grid. A comprehensive procedure is introduced to ensure the quality of the reproduced full-scale sea states. The effect of wave spectrum discretisation techniques and breaking wave algorithms are compared for an optimal performance. The evaluation of the simulation results takes into account the kurtosis and the wave crest distribution in addition to the wave spectra. The vertical arrangement of the σ-coordinate grid plays an important role in representing the dispersion relation and a grid optimisation method is explained. The current study provides a working procedure that reproduces high-fidelity irregular sea states with breaking waves in an efficient FNPF NWT.

Keywords: fully nonlinear potential flow; irregular sea state; breaking wave; σ-coordinate

*Corresponding author, weizhi.wang@ntnu.no
Postprint, published in Applied Ocean Research, doi:http://dx.doi.org/10.1016/j.apor.2021.102898

1 Introduction

In the design of offshore and coastal structures, the global loads and motions are critical considerations as well as mooring line tensions. Quantification of the sea state is the first step in the design process to provide accurate wave inputs. The irregular nature of the ocean requires long duration studies to obtain the statistical properties of a certain sea state such as the significant values, the extreme values and the wave spectrum at both low and high frequency ends of the wave spectrum. Irregular waves consist of many regular wave components with a wide range of frequencies. The low frequency components in an irregular sea contribute to the low-frequency damping for the mooring system and drifting for floating structures (Magnussen, 2014). The high-frequency components usually contribute to very nonlinear resonance phenomena of the structure such as ringing. For extreme sea states, the first- and second-order wave theory is not adequate to represent a correct wave crest distribution. Both Kriebel and Dawson (1991) as well as Forristall (2000*a*) reported significant deviation of a Rayleigh distribution predicted with a linear wave theory. There are few analytical solutions to nonlinear irregular waves and therefore a fully nonlinear irregular sea state analysis relies on numerical simulations. A well-designed numerical tool should take into account the complete range of frequencies, the wave crest height distribution due to the nonlinearity as well as wave breaking. A phase-resolved solution is required for the time domain analysis of structural response, and thus the numerical model is supposed to be computationally efficient in order to provide a time series for the standard practice of three hours (Huang and Guo, 2017).

Several numerical models of different types have been developed to simulate irregular sea states in the open ocean with constant water depth. Computational fluid dynamics (CFD) models that solve the Naiver-Stokes equations provide comprehensive details of the flow field, from wave kinematics and dynamics to overturning wave breakers and turbulence. Commercial software such as StarCCM+ (CD-adapco, 2016) and ANSYS Fluent (FLUENT, 2017) and open-source codes such as OpenFOAM (OpenFOAM, 2019) and REEF3D::CFD (Bihs et al., 2016) are all widely used CFD tools that represent most of the physical details of ocean waves. However, a full three-hour time series is required by industrial practice in order to provide statistical properties of an irregular sea state (Huang and Guo, 2017). CFD is in general computationally demanding, and such long duration simulations usually require a tremendous mount of computational resources and time. In some cases, it was reported that hundreds of seconds of CFD simulation of an irregular sea state takes up to several days with a multi-processor computational infrastructure (Aggarwal et al., 2018*a*,*b*). As a result, other wave models are preferred for the numerical simulation of irregular sea-states at a much lower computational cost.

Boussinesq-type models (Madsen et al., 1991; Madsen and rensen, 1992; Nwogu, 1993) are also efficient phase-resolving wave modelling alternatives. Though the model was initially developed based on shallow water theory, continuous efforts have been made to represent the dispersion relation in deeper water conditions by increasing the order of the Boussinesq dispersive terms. For example, an accurate representation of dispersion relation up to the water depth to wavelength ratio $kh = 6$ was achieved by Madsen and Schäffer (1998) and Gobbi et al. (2000). Their methods result in up to fifth-order spatial derivatives in an extremely complex equation system, which increases the risk of numerical instabilities. Instead, Madsen et al. (2002) used multiple expansions at various vertical layers of the water column and

reported an accurate representation of the dispersion relation up to $kh = 40$. This multiple expansion results in a large set of equations and an increasing number of unknowns. Taking a different approach, Lynett and Liu (2004) developed a multi-layer approach by dividing the vertical water column into a finite number of layers with quadratic polynomials and matching them at the interfaces. Further development in the multi-layer approach have shown that the flow information in the vertical direction is well resolved with 2-3 layers in deep water conditions (Stelling and Duinmeijer, 2003; Zijlema and Stelling, 2005, 2008; Zijlema et al., 2011). However, Monteban (2016) reported that a two-layer configuration results in about 10 times the computational cost in comparison to a one-layer arrangement, which shows a dramatic increase of computational resources as the layers increase. Jeschke et al. (2017) introduced an innovative quadratic pressure assumption which can achieve at least a good equivalence to a second-order Boussinesq model without multi-layers. Its performance gain over irregular topography was confirmed by Wang et al. (2020). van Groesen et al. (2010) and van Groesen and Andonowati (2007) presented a model based on Korteweg–de Vries (KdV)-type equations and Hamiltonian structure of gravity surface waves. The model is shown to be able to simulation both long and short waves with a large range of water depth variations.

In spite of the continuous efforts of applying numerical models based on shallow water equations to deepwater scenarios, the offshore industry has been preferring the potential flow based numerical models which usually are not limited by water depth conditions due to the nature of the governing equations. Potential flow models solve the Laplace equation together with free surface boundary conditions and the solid-surface boundary conditions at the seabed or the surface of an object. Due to the boundary-value nature of the governing equation, the early potential flow models usually apply the boundary element method (BEM) (Grilli et al., 1994). The BEM models are seen to be computationally efficient and eligible for both constant and varying topographies (Grilli et al., 2001). However, the fully populated unsymmetrical matrix presents a difficulty in implementing high-order numerical schemes and parallel computation techniques. Consequently, the method is computationally sufficient for small domain analyses but not optimal for large-scale applications. Li and Fleming (1997) presented a three dimensional fully nonlinear potential flow model using a finite difference method and a multi-grid solver. Further developments by Bingham and Zhang (2007) and Engsig-Karup and Bingham (2009) resulted in the general purpose flexible-order fully nonlinear potential flow model OceanWave3D. The model is capable of simulating irregular waves as well as different wave transformations. The use of a σ-coordinate grid and a stretching function in the vertical direction further improve the model's computational efficiency as well as its flexibility over varying seabed. A GPU-accelerated version of OceanWave3D was also developed (Engsig-Karup et al., 2012; Glimberg et al., 2013), which dramatically improved the computational efficiency for large-scale long duration simulations. Another fully-nonlinear potential flow code following a similar approach was also implemented at TechnipFMC (Kim and Bai, 1999; Kim et al., 2006). Here, the velocity potential is solved on a σ-coordinate grid with a Chebyshev polynomial interpolation in the vertical direction. The code has been used in the offshore industry for the evaluation of design conditions. High-order spectral (HOS) method is another technique to solve for the velocity potential. Here, the Laplace equation is solved analytically in the volume beforehand so that only the free surface boundary conditions need to be time-integrated. In combination with the use of Fast Fourier Transform (FFT), the HOS models show very high computational efficiency. Successful HOS models have been developed for both experimental scales and large-scales, such as the HOS-NWT and HOS-

Ocean models (Ducrozet et al., 2012; Bonnefoy et al., 2006*a*,*b*) and Whisper3D (Raoult et al., 2016; Yates and Benoit, 2015). However, simple analytical solutions to the Laplace equation exist in constant water depth, but not for more complex bottom topography, an adaption for a varying bathymetry is often required in a HOS model.

With the computational efficiency and the validity for a large range of water depth, potential flow models have been used for long duration sea state simulations. Ducrozet et al. (2012) used HOS-NWT wave maker signal to generate an irregular wave field and focused wave, Bonnefoy et al. (2009) further performed $250T_p$ long-time 3D simulations to detect freak wave occurrence in a 3D domain, with T_p being the peak period. Ducrozet et al. (2007) demonstrated numerical investigation of freak wave in a 2D irregular wave field with $1000T_p$ duration and in a 3D wave field with $250T_p$ duration. Ducrozet et al. (2007) and Duc (2016) used HOS-Ocean to simulate a $250T_p$ 3D irregular wave field with periodic lateral boundary conditions. The finite element fully nonlinear potential flow model from TechnipFMC (Kim and Bai, 1999; Kim et al., 2006) has been applied extensively for the simulation of three-hour sea-states with breaking waves in intermediate to deep water. Huang and Guo (2017); Huang and Zhang (2018) performed three-hour simulations of irregular sea states with many realisations. It is reported that it is very challenging to capture the high-frequency part of the spectrum with a higher steepness $H_s/L_p > 0.2$. A new wave crest distribution formulation was also derived based on the researches to represent the highly nonlinear sea-state. These long duration numerical simulations both provided the research community with benchmark cases and insights for the mathematical representations of the nonlinear irregular sea states. However, a correct representation of an irregular sea state requires adequate attention on many factors, such as the frequency band width, spectrum discretisation, arrangement of the σ-coordinate etc. The previously reported studies are lack of technical details about the numerical wave tank configuration and the choices of parameters, making it hard to reproduce the results when a different numerical model is applied. A common procedure regarding the most important configurations is needed for the researchers who share the interest in irregular sea-state with different wave breaking scenarios.

In order to demonstrate a working procedure for the numerical reproduction of irregular sea state, the fully nonlinear potential flow model REEF3D::FNPF (Bihs et al., 2020) that solve for the velocity potential using a finite difference method on a σ-coordinate grid is used in this article. Developed as an integrated part of the open-source hydrodynamics model REEF3D (Bihs et al., 2016), the potential flow model inherits the high-order numerical discretisation schemes in space and time as well as the high performance computation capacity. The CFD model of REEF3D has been used for the investigation of 2D unidirectional irregular wave field (Aggarwal et al., 2018*b*,*a*) and 3D short-crested wave field (Wang et al., 2018*a*,*b*), which demonstrated its numerical robustness. The potential flow model REEF3D::FNPF was applied to study the geometric properties of rogue waves in deep water (Wang et al., 2019).

In this manuscript, the authors address several key factors that influence the quality of the irregular wave field in a potential flow numerical wave tank on a σ coordinate grid. The goal is to introduce a procedure for a reproducible representation of an irregular sea-state. In section 2, the numerical implementation of the model REEF3D::FNPF is introduced. In section 3, the considerations regarding domain size, probe location, frequency bandwidth, grid resolution, time-stepping and arrangement of the σ coordinate grid are addressed. In section 4, the numerical results are presented, where the effectiveness of the procedure as well as the effects of the different factors are discussed. In the conclusion, the findings are summarised

and a working procedure is produced.

2 Numerical model

2.1 Governing equations

The governing equation for the fully nonlinear potential flow model REEF3D::FNPF is the Laplace equation:

$$\frac{\partial^2 \phi}{\partial x^2} + \frac{\partial^2 \phi}{\partial y^2} + \frac{\partial^2 \phi}{\partial z^2} = 0. \tag{1}$$

Boundary conditions are required in order to solve for the velocity potential ϕ from the Laplace equation, especially at the free surface and at the bottom. The fluid particles at the free surface should always remain at the surfaces, which defines the kinematic free surface boundary condition. The pressure in the fluid at the free surface should be equal to the atmospheric pressure. This describes the dynamic free surface boundary condition. These two conditions must always be fulfilled:

$$\frac{\partial \eta}{\partial t} = -\frac{\partial \eta}{\partial x}\frac{\partial \widetilde{\phi}}{\partial x} - \frac{\partial \eta}{\partial y}\frac{\partial \widetilde{\phi}}{\partial y} + \widetilde{w}\left(1 + \left(\frac{\partial \eta}{\partial x}\right)^2 + \left(\frac{\partial \eta}{\partial y}\right)^2\right), \tag{2}$$

$$\frac{\partial \widetilde{\phi}}{\partial t} = -\frac{1}{2}\left(\left(\frac{\partial \widetilde{\phi}}{\partial x}\right)^2 + \left(\frac{\partial \widetilde{\phi}}{\partial y}\right)^2 - \widetilde{w}^2\left(1 + \left(\frac{\partial \eta}{\partial x}\right)^2 + \left(\frac{\partial \eta}{\partial y}\right)^2\right)\right) - g\eta. \tag{3}$$

where η is the free surface elevation, $\widetilde{\phi} = \phi(\mathbf{x}, \eta, t)$ stands for the velocity potential at the free surface, $\mathbf{x} = (x, y)$ represents the coordinates at the horizontal plane and $\widetilde{w}$ is the vertical velocity at the free surface.

At the bottom, the velocity component normal to the bottom shall always be zero since the fluid particle cannot penetrate the solid boundary. This gives the bottom boundary condition:

$$\frac{\partial \phi}{\partial z} + \frac{\partial h}{\partial x}\frac{\partial \phi}{\partial x} + \frac{\partial h}{\partial y}\frac{\partial \phi}{\partial y} = 0, \quad z = -h. \tag{4}$$

where $h = h(\mathbf{x})$ is the water depth measured from the still water level to the seabed.

Due to the time-dependent nature of the free surface boundary conditions, a time-variant σ-coordinate system (Engsig-Karup and Bingham, 2009) is used for the vertical grid arrangement. The σ-coordinate system allows the vertical grid to follow the water depth variations over space as well as the free surface elevations over time and thus offers great flexibility for irregular boundaries. The transformation from a Cartesian coordinate system to a σ-coordinate system is expressed as follows:

$$\sigma = \frac{z + h\,(\mathbf{x})}{\eta(\mathbf{x}, t) + h(\mathbf{x})}. \tag{5}$$

The velocity potential after the σ-coordinate transformation is denoted as Φ in the following context. The boundary conditions and the Laplace equation in the σ-coordinate are then rewritten in the following format:

$$\Phi = \widetilde{\phi} \qquad ,\sigma = 1; \tag{6}$$

$$\frac{\partial^2\Phi}{\partial x^2} + \frac{\partial^2\Phi}{\partial y^2} + \left(\frac{\partial^2\sigma}{\partial x^2} + \frac{\partial^2\sigma}{\partial y^2}\right)\frac{\partial\Phi}{\partial\sigma} + 2\left(\frac{\partial\sigma}{\partial x}\frac{\partial}{\partial x}\left(\frac{\partial\Phi}{\partial\sigma}\right) + \frac{\partial\sigma}{\partial y}\frac{\partial}{\partial y}\left(\frac{\partial\Phi}{\partial\sigma}\right)\right) + \left(\left(\frac{\partial\sigma}{\partial x}\right)^2 + \left(\frac{\partial\sigma}{\partial y}\right)^2 + \left(\frac{\partial\sigma}{\partial z}\right)^2\right)\frac{\partial^2\Phi}{\partial\sigma^2} = 0 \quad ,0 < \sigma < 1; \tag{7}$$

$$\left(\frac{\partial\sigma}{\partial z} + \frac{\partial h}{\partial x}\frac{\partial\sigma}{\partial x} + \frac{\partial h}{\partial y}\frac{\partial\sigma}{\partial y}\right)\frac{\partial\Phi}{\partial\sigma} + \frac{\partial h}{\partial x}\frac{\partial\Phi}{\partial x} + \frac{\partial h}{\partial y}\frac{\partial\Phi}{\partial y} = 0 \qquad ,\sigma = 0. \tag{8}$$

where $\sigma = 1$ corresponds to the free surface and $\sigma = 0$ corresponds to the bottom. Once the velocity potential Φ is obtained in the σ-coordinate system, the velocities can be calculated:

$$u(\mathbf{x}, z) = \frac{\partial\Phi(\mathbf{x}, z)}{\partial x} = \frac{\partial\Phi(\mathbf{x}, \sigma)}{\partial x} + \frac{\partial\sigma}{\partial x}\frac{\partial\Phi(\mathbf{x}, \sigma)}{\partial\sigma}, \tag{9}$$

$$v(\mathbf{x}, z) = \frac{\partial\Phi(\mathbf{x}, z)}{\partial y} = \frac{\partial\Phi(\mathbf{x}, \sigma)}{\partial y} + \frac{\partial\sigma}{\partial y}\frac{\partial\Phi(\mathbf{x}, \sigma)}{\partial\sigma}, \tag{10}$$

$$w(\mathbf{x}, z) = \frac{\partial\Phi(\mathbf{x}, z)}{\partial z} = \frac{\partial\sigma}{\partial z}\frac{\partial\Phi(\mathbf{x}, \sigma)}{\partial\sigma}. \tag{11}$$

The Laplace equation is discretised using second-order central differences on a σ-coordinate system (Engsig-Karup and Bingham, 2009) and solved using a parallelised geometric multigrid preconditioned conjugated gradient solver provided by Hypre (van der Vorst, 1992).

The gradient terms of the free-surface boundary conditions are discretised with the $5th$-order Hamilton-Jacobi version of the weighted essentially non-oscillatory (WENO) scheme (Jiang and Shu, 1996). The WENO stencil consists of three local essentially non-oscillatory (ENO)-stencils and each is assigned with a smoothness indicators IS (Jiang and Shu, 1996). A large IS indicates a non-smooth solution in a local stencil. The scheme is designed so that the local stencil with the highest smoothness (i.e. smallest IS) is assigned with the largest weight ω_i and therefore contributes the most. In this way, the scheme is able to handle large gradients up to shock with good accuracy. The WENO approximation for Φ is a convex combination of the three possible ENO approximations. For example, the schematic of the WENO stencils in the x-direction with a convective velocity from left to right is shown in Fig. 1.

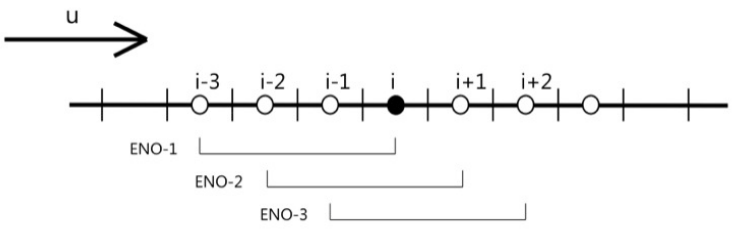

Figure 1: Schematic of a 5th-order WENO stencil.

The discretisation is formulated as the following:

$$\Phi_x^{\pm} = \omega_1^{\pm}\Phi_x^{1\pm} + \omega_2^{\pm}\Phi_x^{2\pm} + \omega_3^{\pm}\Phi_x^{3\pm}. \tag{12}$$

The three stencils are defined as:

$$\begin{aligned}
\Phi_x^{\pm} &= \frac{1}{3}q_1^{\pm} - \frac{7}{6}q_2^{\pm} + \frac{11}{6}q_3^{\pm}, \\
\Phi_x^{\pm} &= -\frac{1}{6}q_2^{\pm} + \frac{5}{6}q_3^{\pm} + \frac{1}{3}q_4^{\pm}, \\
\Phi_x^{\pm} &= \frac{1}{3}q_3^{\pm} + \frac{5}{6}q_4^{\pm} - \frac{1}{6}q_5^{\pm}.
\end{aligned} \tag{13}$$

with

$$\begin{aligned}
q_1^- &= \frac{\Phi_{i-2} - \Phi_{i-3}}{\Delta x}, q_2^- = \frac{\Phi_{i-1} - \Phi_{i-2}}{\Delta x}, q_3^- = \frac{\Phi_i - \Phi_{i-1}}{\Delta x}, \\
q_4^- &= \frac{\Phi_{i+1} - \Phi_i}{\Delta x}, q_5^- = \frac{\Phi_{i+2} - \Phi_{i+1}}{\Delta x}
\end{aligned} \tag{14}$$

and

$$\begin{aligned}
q_1^+ &= \frac{\Phi_{i+3} - \Phi_{i+2}}{\Delta x}, q_2^+ = \frac{\Phi_{i+2} - \Phi_{i+1}}{\Delta x}, q_3^+ = \frac{\Phi_{i+1} - \Phi_i}{\Delta x}, \\
q_4^+ &= \frac{\Phi_i - \Phi_{i-1}}{\Delta x}, q_5^+ = \frac{\Phi_{i-1} - \Phi_{i-2}}{\Delta x}
\end{aligned} \tag{15}$$

The weights are written as

$$\omega_1^{\pm} = \frac{\alpha_1^{\pm}}{\alpha_1^{\pm} + \alpha_2^{\pm} + \alpha_3^{\pm}}, \omega_2^{\pm} = \frac{\alpha_2^{\pm}}{\alpha_1^{\pm} + \alpha_2^{\pm} + \alpha_3^{\pm}}, \omega_3^{\pm} = \frac{\alpha_3^{\pm}}{\alpha_1^{\pm} + \alpha_2^{\pm} + \alpha_3^{\pm}} \tag{16}$$

and

$$\alpha_1^{\pm} = \frac{1}{10}\frac{1}{\left(\widetilde{e} + IS_1^{\pm}\right)^2}, \alpha_2^{\pm} = \frac{6}{10}\frac{1}{\left(\widetilde{e} + IS_2^{\pm}\right)^2}, \alpha_3^{\pm} = \frac{3}{10}\frac{1}{\left(\widetilde{e} + IS_3^{\pm}\right)^2} \tag{17}$$

with the regularisation parameter $\widetilde{e} = 10^{-6}$ and the following smoothness indicators:

$$
\begin{aligned}
IS_1^{\pm} &= \frac{13}{12}\left(q_1 - 2q_2 + q_3\right)^2 + \frac{1}{4}\left(q_1 - 4q_2 + 3q_3\right)^2, \\
IS_2^{\pm} &= \frac{13}{12}\left(q_2 - 2q_3 + q_4\right)^2 + \frac{1}{4}\left(q_2 - q_4\right)^2, \\
IS_3^{\pm} &= \frac{13}{12}\left(q_3 - 2q_4 + q_5\right)^2 + \frac{1}{4}\left(3q_3 - 4q_4 + q_5\right)^2,
\end{aligned}
\tag{18}
$$

For the temporal discretisation of the time-dependent terms in the free surface boundary conditions, a third-order accurate total variation diminishing (TVD) Runge-Kutta scheme (Shu and Osher, 1988) is used that consists of three Euler steps (Shu and Osher, 1988).

$$
\begin{aligned}
\phi^{(1)} &= \phi^n + \Delta t L\left(\phi^n\right) \\
\phi^{(2)} &= \frac{3}{4}\phi^n + \frac{1}{4}\phi^{(1)} + \frac{1}{4}\Delta t L\left(\phi^{(1)}\right) \\
\phi^{n+1} &= \frac{1}{3}\phi^n + \frac{2}{3}\phi^{(2)} + \frac{2}{3}\Delta t L\left(\phi^{(2)}\right)
\end{aligned}
\tag{19}
$$

The numerical workflow of solving the Laplace equation and boundary conditions for ϕ and η within in one Runge-Kutta step is summarised in Fig. 2

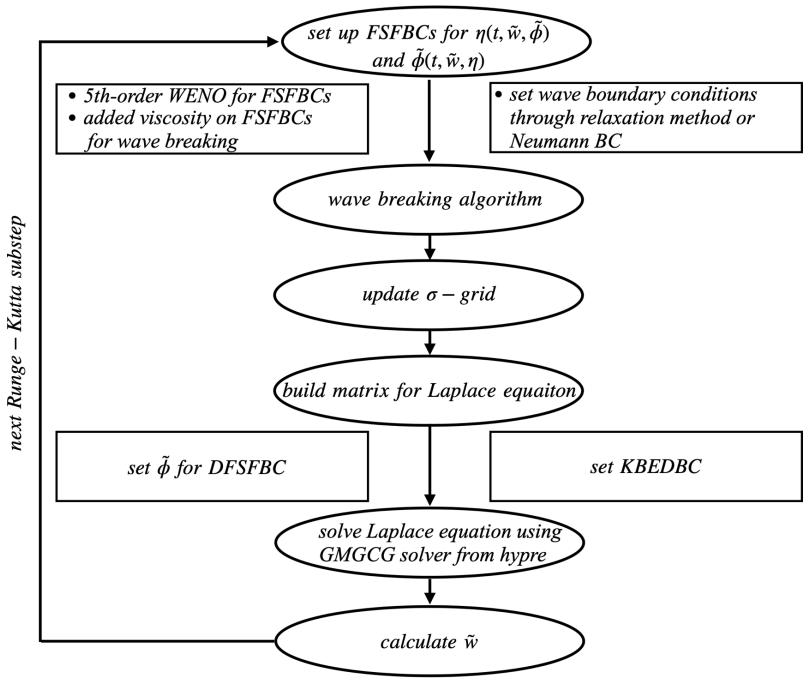

Figure 2: Numerical workflow of solving the Laplace equation and boundary conditions for the velocity potential ϕ and free surface elevation η within in one Runge-Kutta sub-step.

The efficient computation of long duration simulations depends largely on the strategy for the computational parallelisation. In REEF3D, parallelisation is achieved through domain decomposition, where the simulation domain is divided into smaller sub-domains, each of them

communicating with their adjacent neighbours through ghost cells. Since a 5th-order WENO scheme is used for the free surface boundary conditions, three ghost cell levels are required to complete the stencils. The message passing interface (MPI) is used for the implementation of the ghost cell value exchange. The strategy of ghost cell-based domain decomposition and MPI enables the model to perform demanding simulations with hundreds of processors simultaneously.

2.2 Irregular wave generation

Flexible wave generation methods are implemented (Bihs et al., 2016). In this paper, a relaxation method is used for the wave generation with the following relaxation function (Mayer et al., 1998):

$$\Gamma(\widetilde{x}) = 1 - \frac{e^{(\widetilde{x}^{3.5})} - 1}{e - 1} \; for \; \widetilde{x} \in [0; 1], \tag{20}$$

where $\widetilde{x}$ is scaled to the length of the relaxation zone. The velocity potential Φ and the surface elevation η are increased to the analytical values in the wave generation zone:

$$\varphi(\widetilde{x})_{relaxed} = \Gamma(\widetilde{x})\varphi_{analytical} + (1 - \Gamma(\widetilde{x}))\varphi_{computational}, \tag{21}$$

Similarly, the velocity potential and the surface elevation η are reduced to still water values in the wave energy dissipation zone or numerical beach to eliminate wave reflection of the outlet boundaries.

The irregular wave generation is achieved by a linear superposition of a finite number of individual regular wave components with different amplitudes, frequencies and phases. Assuming that each wave component is a linear wave, the first-order free surface $\eta^{(1)}$ is defined as

$$\eta^{(1)} = \sum_{i=1}^{N} A_i \cos\theta_i. \tag{22}$$

where A_i is the amplitude of each wave component and θ_i is the phase of each component, which is defined as

$$\theta_i = k_i x - \omega_i t - \varepsilon_i. \tag{23}$$

where k_i is the wave number, ω_i is the angular frequency, ε is the phase of each wave component.

A power spectrum is used to describe the energy distribution over the frequencies. A commonly used power spectrum for the North Sea marine environment is the JONSWAP spectrum (DNV, 2011). Significant wave height H_s, peak angular frequency ω_p, and number of components N are given as input values to the JONSWAP spectrum (DNV, 2011):

$$S(\omega) = \frac{5}{16} H_s^2 \omega_p^4 \omega_i^{-5} exp\left(-\frac{5}{4}\left(\frac{\omega_i}{\omega_p}\right)^{-4}\right) \gamma^{exp\left(\frac{-(\omega-\omega_p)^2}{2\sigma^2\omega_p^2}\right)} A_\gamma. \tag{24}$$

where the peak-shape parameter $\gamma = 3.3$ and the spectral width parameter σ is 0.07 for $\omega_i \leq \omega_p$ and 0.09 for $\omega_i > \omega_p$. The normalising facor $A_\gamma = 1 - 0.287ln(\gamma)$.

When a frequency range is chosen between a low frequency end ω_s and a high-frequency end ω_e, a finite number of discrete frequencies (N_f) are needed to sufficiently represent the wave energy described by the power spectrum. Two methods to choose the frequency components are presented in this paper: the peak enhance method (PEM) and the equal energy method (EEM) (Duarte et al., 2014) . In PEM, the frequency range is divided at the peak frequency (ω_p) into two sub-ranges [ω_s,ω_p] and [ω_p,ω_e]. In the lower and higher ranges of the peak frequency, the frequencies are evenly distributed into N_s and N_e frequency components respectively. It is a variant of the equivalence-distance arrangement of the frequencies while maintaining the location of the peak frequency regardless of how many components are used. The relationship among ω_s,ω_p, ω_e, N_s, N_f and N_e is summarised in Eqn. 25:

$$\begin{aligned} N_f &= N_s + N_e \\ \frac{N_s}{N_e} &= \frac{\omega_p - \omega_s}{\omega_e - \omega_p} \end{aligned} \tag{25}$$

Instead of evenly distributing the frequency components, the EEM method discretises the power spectrum so that the energy at each frequency interval is kept constant. As a result, the frequency intervals themselves are not constant and more components are concentrated near the peak frequency. Since the area below the spectra stands for the energy, a spectrum can be regarded as a 'probability density function' (pdf). An integral over the frequency domain gives a concept corresponding to a 'cumulative probability function' (cdf). Choosing an even interval in the y-axis of the cumulative probability function', the corresponding x-axis values are the discrete frequency components. An example of a JONSWAP spectrum discretised into 50 frequency components using EEM is demonstrated in Fig. 3. The demonstrated JONSWAP spectrum follows the formulation of DNV-GL (DNV, 2011) where $H_s = 0.06$ m, $T_p = 0.9$ s and the peak enhance parameter is 3.3.

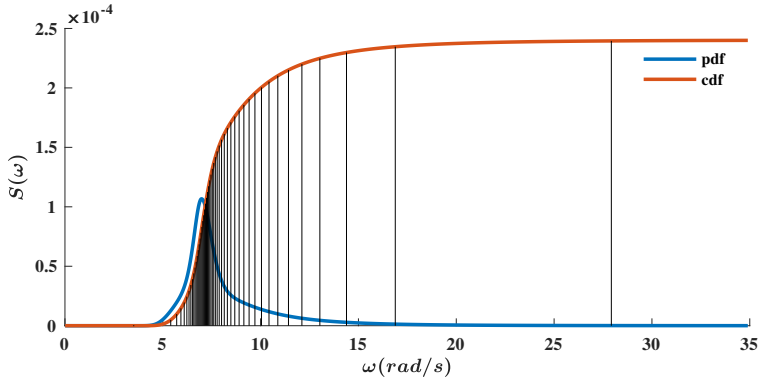

Figure 3: The discretisation of the frequency spectrum based on the Equal Energy method with 50 components

After the discretisation of the power spectrum, the irregular wave free surface elevation is calculated in Eqn. 26:

$$\eta(x,t) = \sum_{I=1}^{N_f} \sqrt{2S(\omega_i)d\omega_i} \cdot \cos(k_i x - \omega_i t + \varepsilon_i) \tag{26}$$

2.3 Wave breaking

Since the free surface is represented by a single value in the presented potential flow model, it is not possible to represent an over-turning breaker as in a CFD simulation (Bihs et al., 2016). However, a correct detection of wave breaking events and energy dissipation can be achieved with an effective breaking wave algorithm. The proposed algorithm aims to address both wave steepness-induced wave breaking in deep water and depth-induced breaking in shallow water.

Deepwater wave steepness-induced breaking is initialised with a steepness criterion:

$$\frac{\partial \eta}{\partial x_i} \geq \beta. \tag{27}$$

where β is the threshold of wave slope at the wave front.

The depth-induced wave breaking is initialised when the vertical velocity of the free-surface exceeds a fraction of the shallow water celerity (Smit et al., 2013):

$$\frac{\partial \eta}{\partial t} \geq \alpha_s \sqrt{gh}. \tag{28}$$

$\alpha_s = 0.6$ is recommended as it works well with most of the waves (Smit et al., 2013).

After a wave breaking is detected, two methods are available to represent the energy dissipation during the wave breaking process. The first method is a geometric filtering algorithm that smoothens the free surface for energy dissipation (Jacobsen, 2011). Here, an explicit scheme is used and therefore there is no Courant-Friedrichs-Lewy (CFL) constraint on the tilmestep size. Another method is to introduce a viscous damping term in the free surface boundary conditions locally around the breaking region as defined by Baquet et al. (2017). When wave breaking is detected, the free surface boundary conditions Eqn. 2 and Eqn. 3 then become:

$$\frac{\partial \eta}{\partial t} = -\frac{\partial \eta}{\partial x}\frac{\partial \widetilde{\phi}}{\partial x} - \frac{\partial \eta}{\partial y}\frac{\partial \widetilde{\phi}}{\partial y} + \widetilde{w}\left(1 + \left(\frac{\partial \eta}{\partial x}\right)^2 + \left(\frac{\partial \eta}{\partial y}\right)^2\right) + \nu_b\left(\frac{\partial^2 \eta}{\partial x^2} + \frac{\partial^2 \eta}{\partial y^2}\right), \tag{29}$$

$$\frac{\partial \widetilde{\phi}}{\partial t} = -\frac{1}{2}\left(\left(\frac{\partial \widetilde{\phi}}{\partial x}\right)^2 + \left(\frac{\partial \widetilde{\phi}}{\partial y}\right)^2 - \widetilde{w}^2\left(1 + \left(\frac{\partial \eta}{\partial x}\right)^2 + \left(\frac{\partial \eta}{\partial y}\right)^2\right)\right) - g\eta + \nu_b\left(\frac{\partial^2 \phi}{\partial x^2} + \frac{\partial^2 \phi}{\partial y^2}\right). \tag{30}$$

where ν_b is the artificial turbulence viscosity. ν_b is calibrated from the comparison of the potential flow model simulations with model test data and the CFD simulations. As a result, the value of ν_b is recommended to be 1.86 (Baquet et al., 2017) for the offshore deep water conditions in the proposed model. In the new free surface boundary conditions Eqn. 29 and Eqn. 30, the newly introduced diffusion term is treated with an implicit time scheme while the

rest of the terms are treated with explicit time schemes. This way, there is no extra constraint on time step size.

A visual comparison of the two methods in the simulation of a wave breaker in an irregular sea state is shown in Fig. 4, where it is seen that both methods show a similar crest height as the CFD counterpart, but the damping method shows a more similar representation of the breaker geometry in comparison to the CFD free surface. The sea state is described by a JONSWAP spectrum (DNV, 2011) where $H_s = 0.0644$ m, $T_p = 1.5$ s and the peak enhance parameter is 3.3.

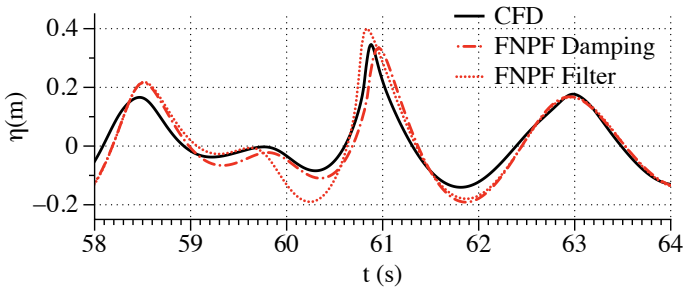

Figure 4: Illustrative comparison of the two wave breaking algorithms with CFD in a simulation of breaking wave event in an irregular sea state.

A correct representation of wave breaking is important for a correct representation of an irregular wave spectrum and the wave crest distribution of a strongly nonlinear irregular sea-state. In the manuscript, both breaking algorithms are used to produce irregular sea-states of moderate and severe breaking scenarios.

2.4 Vertical grid arrangement

In the model, the vertical coordinates follow a stretching function so that smaller cells are arranged near the free surface and larger sizes are closer to the bottom:

$$\sigma_i = \frac{\sinh(-\alpha) - \sinh\left(\alpha\left(\frac{i}{N_z} - 1\right)\right)}{\sinh(-\alpha)}, \tag{31}$$

where α is the stretching factor and i and N_z stand for the index of the grid point and the total number of cells in the vertical direction.

The stretching approach reduces the computational cost as well as the numerical errors when the same number of vertical cells are used. However, the dispersion relation and phase velocity are sensitive to the stretching arrangement. A methodology for an optimal vertical grid distribution is adopted to ensure an accurate representation of the wave propagation.

Since each wave component is a linear wave, the Airy wave theory is used to explain the method. According to the Airy wave theory for infinite water depth, the amplitude of the velocity potential only depends on the vertical coordinate z:

$$\Phi(z) = Ce^{kz}. \tag{32}$$

where $C = A\sqrt{g/k}$, A is the wave amplitude and k is the wave number.

The distribution can be normalised by C to represent a general description. The Taylor expansion of the normalised function $\Phi(z)$ at the free surface ζ up to $3rd$ order can be expressed as the following:

$$e^{kz} = e^{k\zeta} + e^{k\zeta}k\Delta z + \frac{1}{2}e^{k\zeta}k^2\Delta z^2 + \frac{1}{6}e^{k\zeta}k^3\Delta z^3 + O(\Delta z^4). \tag{33}$$

where $\Delta z = z - \zeta$.

The truncation error E is then defined as the difference between the original analytical expression and its Taylor expansion up to the $3rd$ order:

$$E = e^{kz} - \left(e^{k\zeta} + e^{k\zeta}k\Delta z + \frac{1}{2}e^{k\zeta}k^2\Delta z^2 + \frac{1}{6}e^{k\zeta}k^3\Delta z^3\right) \tag{34}$$

It is seen that the truncation error of a finite difference scheme depends on $\Delta z = z - \zeta$. Alternatively, a more general form of Eqn. 34 can be expressed for a finite difference scheme of order O as:

$$0 = Ee^{-k\zeta} - \sum_{n=O+1}^{\infty} \frac{(k\Delta z)^n}{n!} \tag{35}$$

From this expression, each cell size can be calculated in an iterative manner at each location along the water depth, given a value of the truncation error E and the order of the finite difference scheme O. The vertical grid estimated from this process represents the correct distribution of the velocity potential in the vertical wave column and retains the correct wavenumber and the dispersion relation.

3 Methodology

3.1 Frequency range

The choice of frequency range is important for determining a sea-state realistically and accurately. The inclusion of the low frequency and high frequency ranges are important for a correct representation of wave-wave interactions as well as structure responses such as drifting and ringing. The bandwidth of the frequency range also influence the grid resolution in the horizontal direction. An adequate amount of cells per wavelength is usually required to represent a regular wave accurately. In order to represent all wave components that consist the irregular wave field, the grid resolution depends on an adequate amount of cells per wavelength of the shortest regular wave component (with the highest frequency). There are two general principles when choosing the frequency range: 1) wave energy should be represented as much as possible; 2) all wave components in the wave train have to fulfil the linear wave assumption, based on which the irregular wave theory is derived. In this manuscript, the low-frequency end (ω_s) is chosen so that it truncates off only 0.05% of the total wave energy. For the high-frequency end (ω_e), it is chosen either at a frequency that truncates 99% of the wave energy or at the high-frequency limit that the waves fulfil the linear wave theory. The linear wave theory requirement in deep water is:

$$kA = \frac{\omega_e^2}{g}A << 1 \tag{36}$$

$$L(\omega_e) = \sqrt{\frac{g}{A}} \tag{37}$$

Where k is the wave number, ω_e is the angular frequency, g is gravitational acceleration and A is the wave amplitude. Here, $A = H_s/2$. From eqn. 37, the upper limit of the high-frequency ω_e is determined. In the tested cases, this frequency limit corresponds to $2.5\omega_p$ to $3.5\omega_p$ depending on the spectrum and sea state.

3.2 Horizontal resolution

For regular wave propagation, it is seen that about 32 cells per wave length is usually sufficient to represent the free surface accurately in REEF3D::FNPF (Bihs et al., 2020; Wang et al., 2019). For irregular waves, the wavelength of each of the wave components varies very much. Therefore, the grid resolution should be based on the shortest wave in the irregular wave train. The horizontal cell size is decided as the follows:

$$dx = L_e/32, \tag{38}$$

where L_e is the wavelength corresponding to the high frequency limit ω_e. Such resolution is used for all the following simulations.

3.3 Time stepping

A fixed time step is used in this paper. The principle of determining the time step is to ensure that the flow information does not transport more than one horizontal cell size in distance within one time step. In order to ensure that the chosen time step is sufficient for all different waves travelling at different speed, the time step size is determined using the phase velocity of the longest wave:

$$dt = C_s/dx; \tag{39}$$

Where C_s is phase velocity corresponding to the longest wave with the low frequency limit (ω_s). As a result, the time step is determined by using the phase velocity of the longest wave (lowest frequency ω_s) and the cell size that is determined from the shortest wave (highest frequency ω_e).

In summary, the choice of the frequency range determines the choices of horizontal grid and time step size. Together with the vertical grid arrangement using the constant truncation error method, the numerical setup procedure is summarised in Fig. 5.

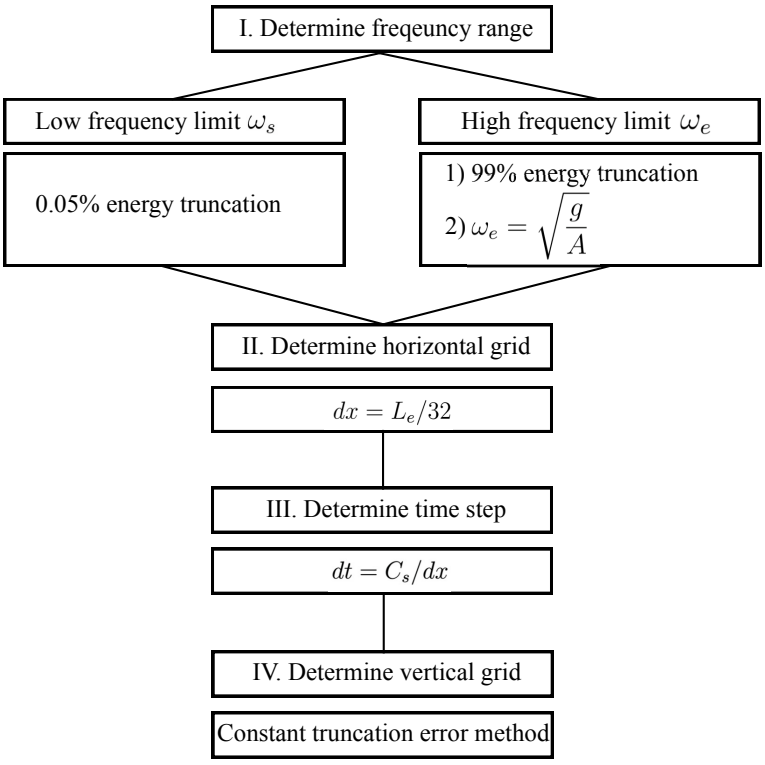

Figure 5: Procedure of the numerical setup for the simulation using a potential flow model with a σ-coordinate grid.

4 Numerical results and discussions

In this section, the methodologies regarding the choices of frequency range, grid resolution and time stepping for the irregular wave representation are put to test. Four different scenarios are presented in the manuscript with various spectra, severity of breaking and water depth. The four scenarios are: non-breaking wave defined with a JONSWAP spectrum (DNV, 2011) in deep water (JNB), mildly breaking wave defined with a JONSWAP spectrum in intermediate water (JMB), severely breaking wave defined with a JONSWAP spectrum in deep water (JSB) and severely-breaking wave defined with an extreme Torsethaugen spectrum (Torsethaugen, 1993, 1996; Torsethaugen and Haver, 2004) in deep water (TSB). The input wave parameters are included in Table. 1. Here, γ is the shape parameter of the JONSWAP spectra, d stands for still water level, $0.5H_sK_p$ is the characteristic wave steepness and ω is the frequency range used in the simulations.

Table 1: Wave conditions for the simulated sea states

Case No.	H_s (m)	T_p (s)	$S(f)$	γ	d (m)	$0.5H_sK_p$	ω (Hz)
JNB	6.21	12.50	JONSWAP	1.2	600.0	0.08	[0.051, 0.283]
JMB	12.25	16.0	JONSWAP	2.5	100.0	0.12	[0.040, 0.201]
JSB	15.64	15.0	JONSWAP	2.5	600.0	0.14	[0.043, 0.178]
TSB	14.60	14.0	Torsethaugen	N/A	600.0	0.15	[0.037, 0.184]

The computational domain is chosen so that all wave components have sufficient space to propagate and develop. Therefore, the domain size is governed by the longest wave component L_{max} corresponding to the lowest frequency. In the numerical wave tank configuration, a wave generation zone of one L_{max} is located at the inlet boundary, and a numerical damping zone of two L_{max} is located at the outlet boundary. The computational zone in between has a length of $11L_{max}$. 7 wave gauges are arranged along the numerical wave tank. The locations of the wave gauges are determined based on the peak wave length L_p corresponding to the peak period T_p, as the wave gauges are designed for the measurement of the characteristic properties of the wave field. Wave gauges G1 and G2 are located at $0.5L_p$ to the upstream side and the downstream side of the boundary between the wave generation zone and the computational zone. Wave gauge G5 is located at $12.5L_p$ from the beginning of the computational domain, with G3 and G4 located $2.5L_p$ and $1.25L_p$ to the upstream of G5 and G6 and G7 located $1.25L_p$ and $2.5L_p$ to the downstream of G5. The principle is that the wave gauges should be located at a sufficient distance away from the wave generation zone so that the wave-wave interactions between the different frequencies have evolved sufficiently. An empirical rule of thumb is that $10L_p$ away from the wave generation should be sufficient for most cases. In this manuscript, the wave gauges cover a range from $10L_p$ to $15L_p$ and the data measured at G5 is considered as the primary measuring point, and its adjacent wave gauges provide information of the spatial variance of the statistical properties of the wave field and provide the evidence that the wave field is fully developed at $12.5L_p$.

Figure 6: Numerical wave tank setup for the irregular wave simulations.

As described previously, the vertical grid arrangement in the σ-coordinate system is important in the quality of the reproduced irregular wave field. Based on the peak period and water depth, the methodology explained in section 2.4 is used to determine the vertical grid for each scenarios. The agreement between the theoretical arrangement and the stretching function within one wavelength in the vertical direction is the criterion in the study as the dispersion relation over one wavelength in the water depth has less impact. Meanwhile, 8 vertical grids are kept within the wavelength correspond to the highest frequency so that the shortest wave component has the grid resolution for its dispersion relation close to the free surface. Keeping a constant truncation error, the theoretical optimal vertical stretchings and

398 the configurations in the numerical model for the four scenarios are illustrated in Fig. 7.

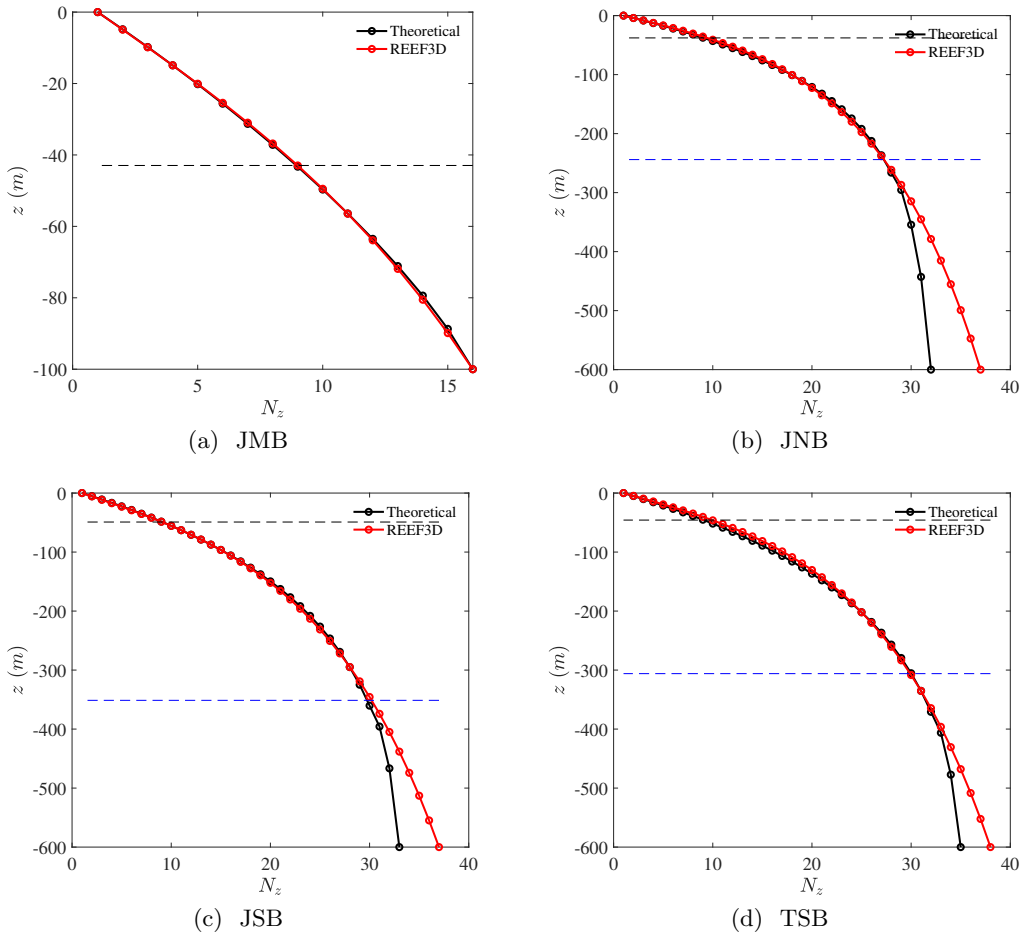

Figure 7: Comparison between theoretical optimal vertical grid arrangement with the actual arrangement in the numerical model based on peak period and water depth using the constant truncation error method (Pakozdi et al., 2019). The black dashed horizontal lines show one wavelength of the highest frequency under the free surface, the blue dashed horizontal lines show one wavelength of the peak frequency under the free surface. In (a), the wave length of the peak period is longer than the water depth and therefore is not shown in the figure.

399 It is seen that the optimised stretching functions agree well with the theoretical calculation
400 within one wavelength of the peak period in all cases. The resulting number of vertical grid
401 lines N_z and the stretching factors α are summarised in Table. 2.
402 Based on the methodology described in section 3, the horizontal grid number N_x and time
403 steps dt are calculated based on the frequency range. The resulting grid configurations are
404 summarised in Table. 2. All simulation are performed for 12800 s, among which the time
405 window between 2000 s and 12800 s form the 3-hour time series for the analysis. 2000 s is
406 long enough to allow at least 250 wave components with the highest frequency (the slowest
407 propagating wave) to finish propagating though the entire numerical wave tank in all scenarios.
408 All simulations are performed with 128 cores of Intel E5-2683v4 2.1 GHz processors on the

supercomputer Fram. The domain length L_{NWT} and the computational time T_{comp} for each simulation are also included in Table. 2.

Table 2: Numerical configurations for the simulated sea states

Case No.	L_{NWT} (m)	N_x	dt (s)	N_z	α	N_t	T_{comp} (h)
JNB	6030.70	9900	0.020	36	3.3	396016	12.5
JMB	9832.93	8184	0.031	15	1.4	245506	4.72
JSB	8644.22	5634	0.042	36	2.8	225366	4.56
TSB	9066.20	6330	0.034	37	3.05	253202	5.66

With the parallel computation algorithm, the numerical model is able to utilise the computational resources effectively. A scalability test is performed with up to 512 computational cores using the wave inputs of the JNB case on the supercomputer Fram. In order to ensure sufficient number of cells per core, a 3D numerical wave tank with the same longitudinal and vertical dimensions as the JNB case is used. It has 10050 cells in the x-direction, 28 cells in the y-direction and 36 cells in the vertical direction. This results in a total of 10.13 million cells, about 20000 cells per core for the 512-core simulation. All simulations are performed for 1000 iterations. The computational speed-up factor defined by the ratio between the simulation time with single-core T_1 and the simulation time with multi-core T_n is plotted in relation to the number of cores. A near linear scalability is seen in Fig. 8.

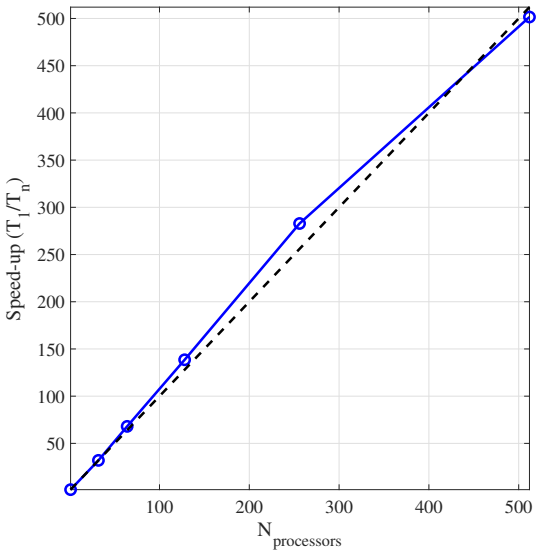

Figure 8: Computational speed-up in relation to the increase of the number of computer cores in the scalability test for the numerical model.

In addition to the general procedure and process for the irregular waves numerical wave tank configurations, the two wave spectrum discretisation methods, the equal energy method (EEM) and the peak enhanced equal distant method (PEM), are tested in the study to investigate their effects on the statistical properties of the wave field. 2480 frequency components are used in all tests based on a Fast Fourier Transform (FFT) analysis of a general equal distance

method (frequencies all evenly distributed through the range without peak enhancing). The two breaking wave algorithms for potential flow solver, the geometric filtering algorithm and the viscous damping algorithm, are also tested. The comparative study on the discretisation method and the breaking wave algorithms are aimed to further help researchers choose the right procedure for an accurate reproduction of an irregular wave field. In the simulation of the non-breaking case JNB, the breaking algorithms are also in use to ensure a compararble numerical set-up as other cases, though wave breakings are not detected during the simuaiton.

4.1 Kurtosis

The first step to check the quality of a numerically reproduced irregular sea state is study the kurtosis of the times series at the points of measurement. If the time series at all measured locations shows a stable and near constant kurtosis, it means that the sea state is spatially homogenous and that the wave gauges are spaced far enough to allow a sufficient wave-wave interaction. In the other case when the kurtosis varies, it shows that the wave field is still developing and wave-wave interaction is undergoing, indicating that a non-homogenous and not fully developed sea. The kurtosis at all wave gauges in all situations are shown in Fig. 9 and Fig. 10.

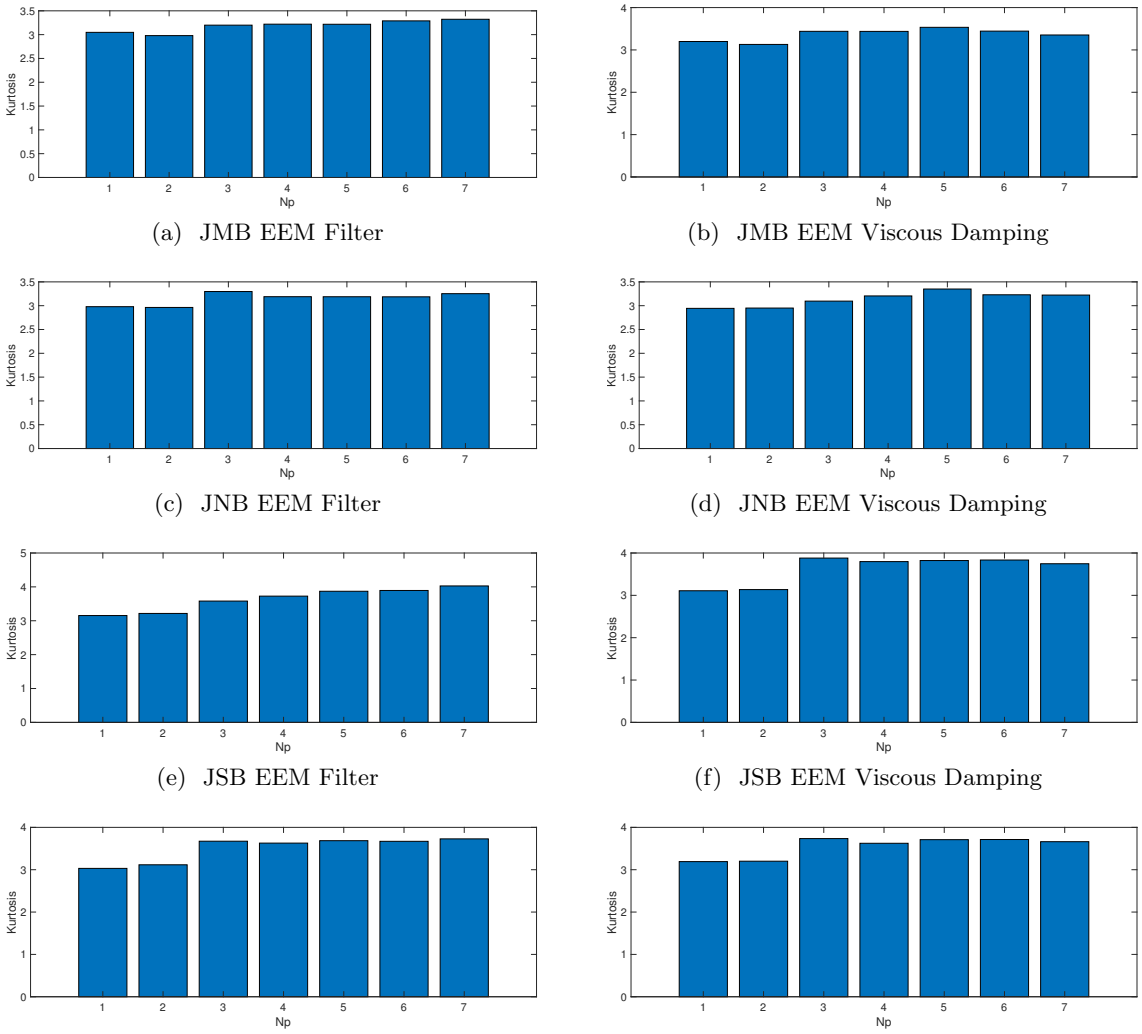

(a) JMB EEM Filter

(b) JMB EEM Viscous Damping

(c) JNB EEM Filter

(d) JNB EEM Viscous Damping

(e) JSB EEM Filter

(f) JSB EEM Viscous Damping

(g) TSB EEM Filter

(h) TSB EEM Viscous Damping

Figure 9: Kurtosis at all wave gauges in the simulations with an EEM method together with the two different wave breaking algorithms.

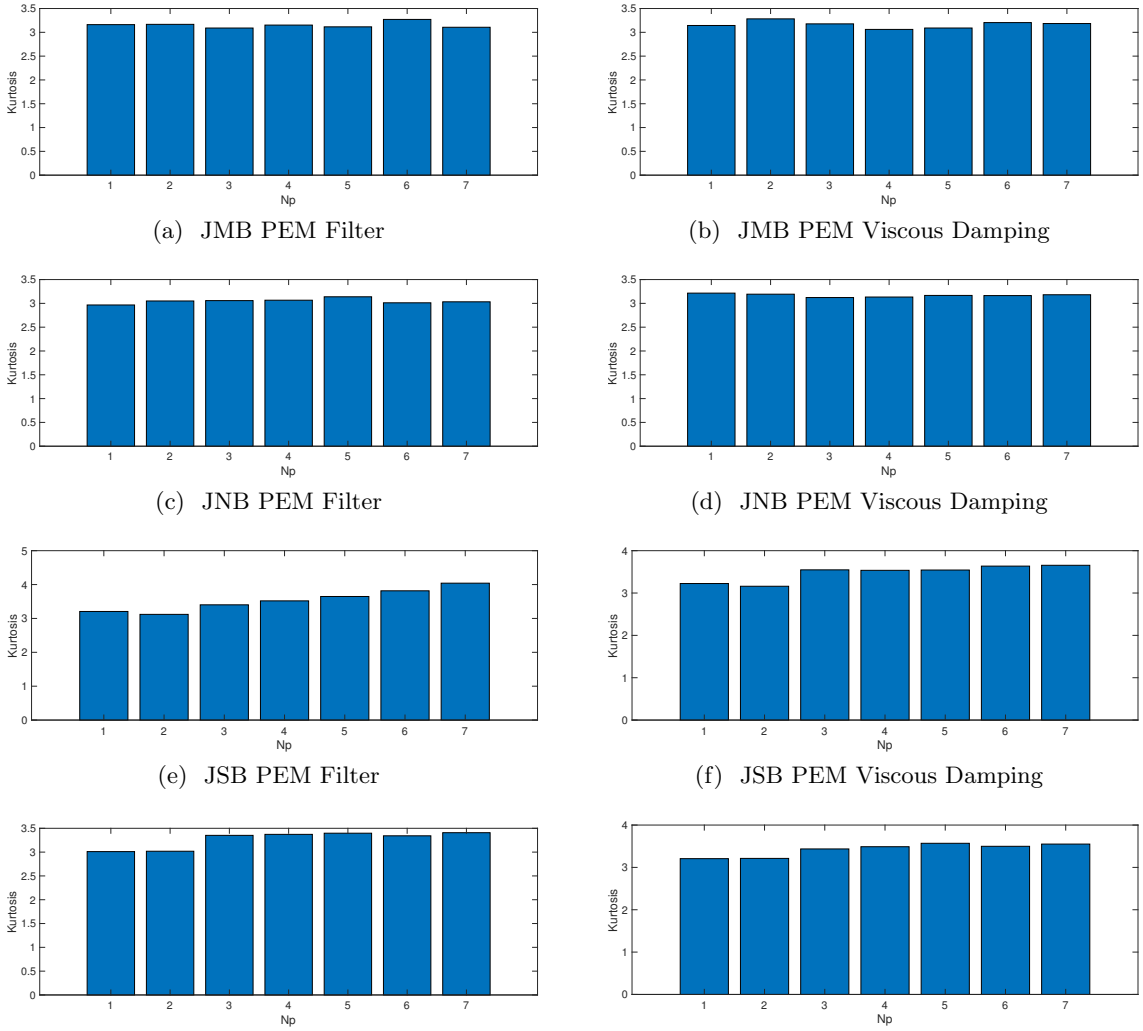

(a) JMB PEM Filter (b) JMB PEM Viscous Damping

(c) JNB PEM Filter (d) JNB PEM Viscous Damping

(e) JSB PEM Filter (f) JSB PEM Viscous Damping

(g) TSB PEM Filter (h) TSB PEM Viscous Damping

Figure 10: Kurtosis at all wave gauges in the simulations with an PEM method together with the two different wave breaking algorithms.

As can be seen, the first two wave gauges G1 and G2 tend to show much smaller kurtosises than the rest of the wave gauges. For the generation of a single frequency regular wave, the waves near the generation zone should be the most accurate in comparison to the input theoretical wave. However, for the irregular wave field, the adjacent area near the generation zone does not allow a sufficient space for the wave-wave interaction to develop and the measurements near the wave generation zone are in fact the least accurate in comparison to the input wave spectrum, as most spectra are formulated for developed sea states. The other five wave gauges located $10L_p$ to $15L_p$ away from the wave generation zone show stable kurtosises with a slight fluctuation around the value 3. This shows that the waves are well developed and the wave gauges are located in the correct place. In general, the spectrum discretisation methods and the breaking wave algorithms do not have a strong impact on the kurtosis. One exception is the JSB case with the geometric filtering algorithm, where the

kurtosis is constantly increasing over the space. It shows that in this severe wave breaking scenario, the viscous damping breaking algorithm is a more stable choice.

4.2 Wave spectra

With the information of a developed sea after $10L_p$, the time series at G5 ($12.5L_p$) is used for reproducing the input wave spectrum. The quality of the reproduced wave spectrum is the most commonly used criterion to examine a numerical simulated irregular sea state. Here, the numerical wave spectra are compared with the input theoretical wave spectra for all simulated cases in Fig. 11 and Fig. 12

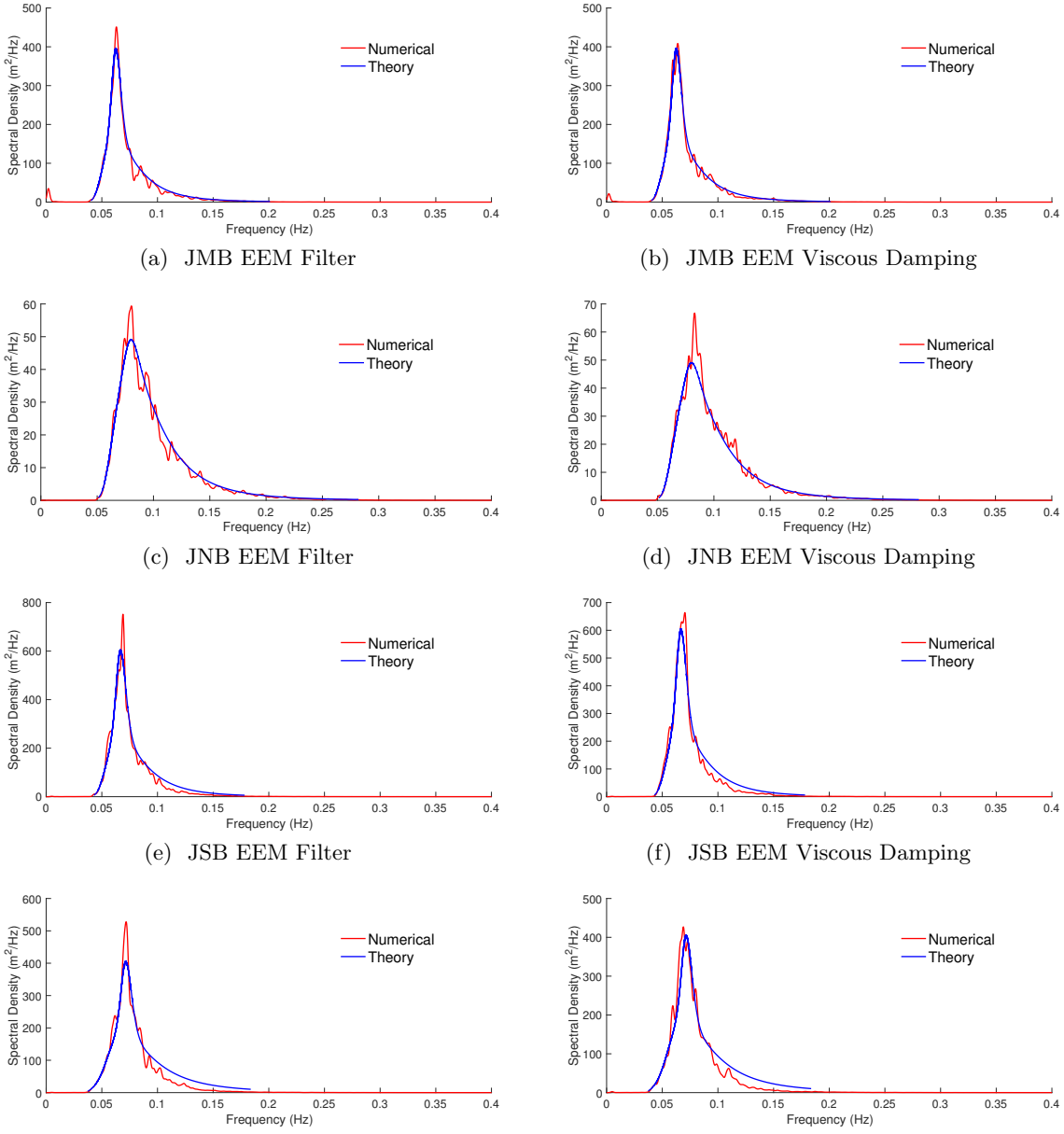

(a) JMB EEM Filter

(b) JMB EEM Viscous Damping

(c) JNB EEM Filter

(d) JNB EEM Viscous Damping

(e) JSB EEM Filter

(f) JSB EEM Viscous Damping

(g) TSB EEM Filter

(h) TSB EEM Viscous Damping

Figure 11: Comparison of the numerically reproduced wave spectra and the input theoretical wave spectra in all cases using the EEM discretisation method.

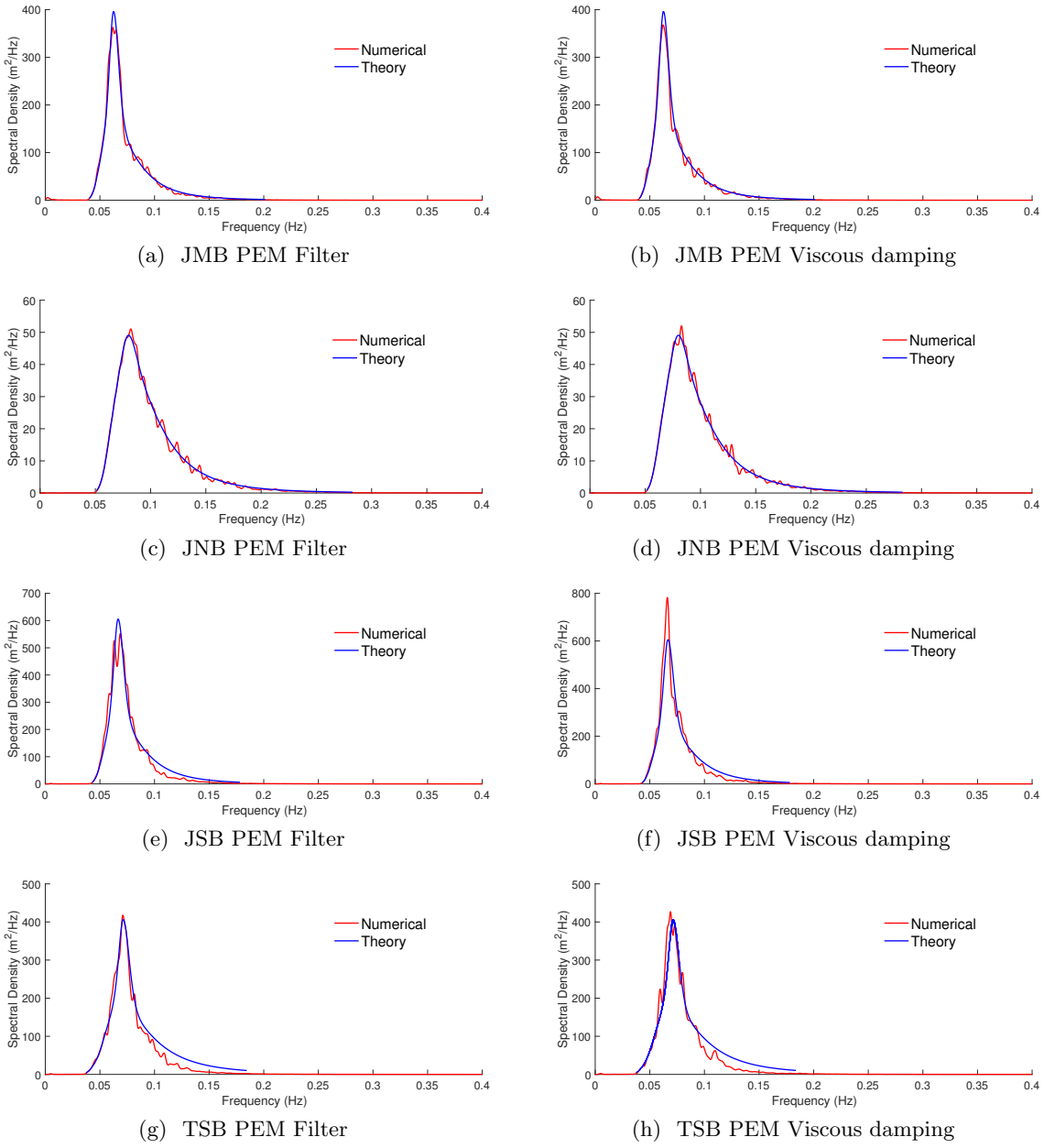

(a) JMB PEM Filter

(b) JMB PEM Viscous damping

(c) JNB PEM Filter

(d) JNB PEM Viscous damping

(e) JSB PEM Filter

(f) JSB PEM Viscous damping

(g) TSB PEM Filter

(h) TSB PEM Viscous damping

Figure 12: Comparison of the numerically reproduced wave spectra and the input theoretical wave spectra in all cases using the PEM discretisation method.

The non-breaking case JNB in deep water shows a near identical agreement at low frequency, peak frequency as well as high frequency range with the PEM method. However, there tends to be a slight overshoot near the peak frequency when the EEM method is applied. One possible reason is that the equal energy bins are too densely allocated near the peak frequency and lead to a slight higher energy concentration. The JMB cases also show near identical agreement in all simulations. Especially, there is no energy loss at the high frequency domain, which indicates the right amount of energy dissipation due to the mild

breaking captured by both breaking algorithms. However, there is a slight underestimation of the spectrum peak when PEM method is used, and a slight overshoot when EEM is used. For the severely breaking cases JSB and TSB, the numerical spectra at the low frequency and peak frequency range agree well with the inputs. Slightly higher energy concentrations near the peak frequency are also observed when the EEM method is applied. At the high-frequency range, certain losses of energy are observed with the JONSWAP spectrum and more prominent energy losses are seen with the Torsethaugen spectrum. Both breaking wave algorithms show similar impact on the wave spectrum, except that when both PEM and filtering algorithms are applied to the JSB case, there is a loss of energy near the peak period in addition to the high-frequency domain. This may be a direct result of a varying kurtosis as seen in section 4.1. Huang and Zhang (2018) also expressed the difficulty in representing the high-frequency range of a wave spectrum for severe wave breaking scenarios. The fundamental reason behind this energy loss still remains as a future research topic. However, the general good agreements in all cases, from non-breaking to sever-breaking show that the procedure presented in the manuscript represent the irregular sea state well in the numerical wave tank.

4.3 Wave crest distribution

Traditionally, a wave spectrum is used to calibrate waves as a defining criterion. However, this criterion is not sufficient. In cases of local wave-structure interactions, such as wave impact on hulls, green water and air gap, wave crest distributions are a necessity to ensure there is no unrealistic wave crest in the numerical wave field (Huang and Zhang, 2018). The traditional Forristall distribution (Forristall, 2000*b*) is derived from linear and second-order wave theory and therefore is not optimal for severe sea state (Baquet et al., 2017). Since most wave crest distributions are developed for the JONSWAP spectrum, the wave crest distribution at wave gauges G3-G5 from all JONSWAP cases are compared to both the Forristall distribution and the distribution suggested by Huang and Zhang (2018) in Fig. 13 and Fig. 14.

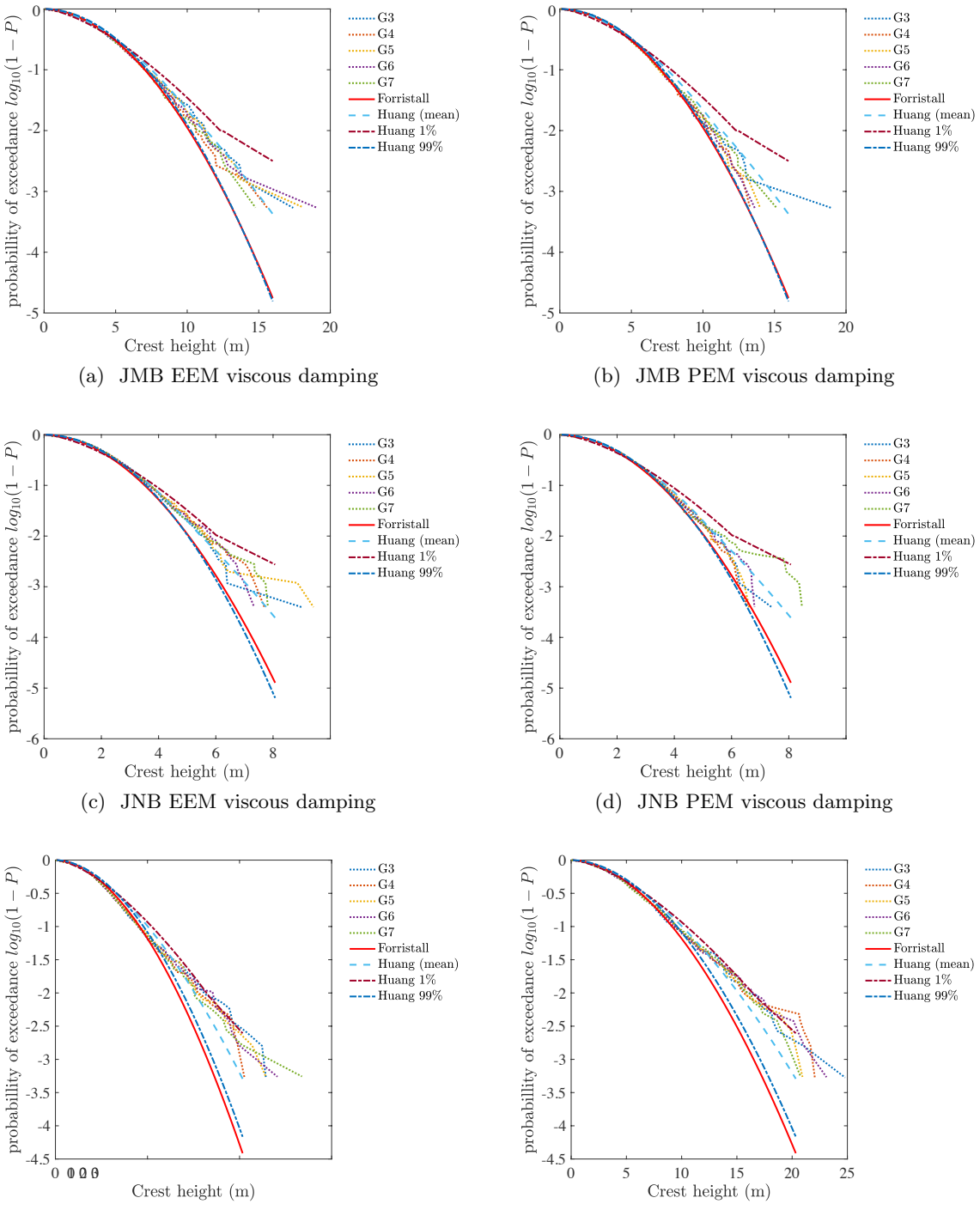

(a) JMB EEM viscous damping

(b) JMB PEM viscous damping

(c) JNB EEM viscous damping

(d) JNB PEM viscous damping

(e) JSB EEM viscous damping

(f) JSB PEM viscous damping

Figure 13: Wave crest distribution at G3-G5 for all cases with the viscous damping wave braking algorithm.

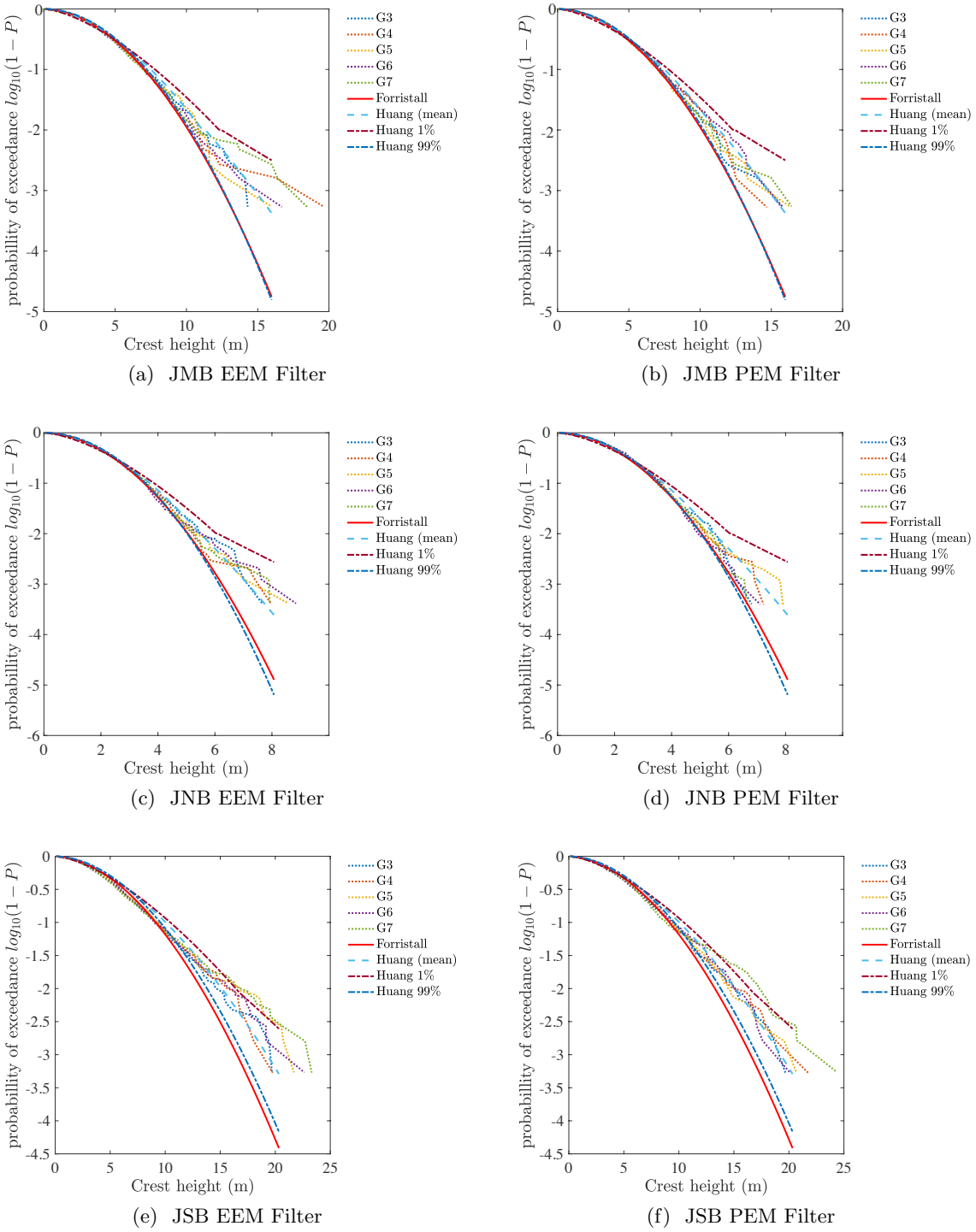

(a) JMB EEM Filter (b) JMB PEM Filter

(c) JNB EEM Filter (d) JNB PEM Filter

(e) JSB EEM Filter (f) JSB PEM Filter

Figure 14: Wave crest distribution at G3-G5 for all cases with the geometric filtering algorithm.

494 It is seen that the difference between the Forristall distribution and the lower bound

of Huang distribution increases with increasing nonlinearity and severity of wave breaking. Huang and Guo (2017) suggested that if a wave realisation generated in a NWT has a crest distribution that falls between the upper and lower bounds, as well as matches the specified target Hs, Tp and spectrum, then it is qualified for model tests. The wave crest distributions of the computed wave fields in the presented simulations are all within the theoretical Forristall distribution and the lower bound of the Huang distribution. It means that the simulated wave fields never underestimate the wave crests, making the sub-consequent design lay on the safe side. For the non-breaking wave case and the mild wave breaking case, the wave crest distributions are well within both the upper and lower bounds of the Huang distribution, fulfilling Huang's qualification criterion (Huang and Guo, 2017). In addition, it is also seen that for the mild wave breaking case JMB, the viscous damping method keeps the wave crest distribution well within the upper and lower limit, while the filtering algorithm tends to have higher crests and a tendency to exceed the upper bound especially when it is used together with the EEM spectrum discretisation method. For the severe wave breaking case JSB, the wave crest distributions at some wave gauges tend to exceed the upper bound with both breaking wave algorithms. This is in contrast to the fact that the high-frequency wave energy is underestimated with severe wave breaking, as seen in Fig. 11 and Fig. 12. The overestimation of the wave crest indicates there might be a need for a stricter wave breaking criterion or slightly more energy dissipation. Under this assumption, the underestimation of the high-frequency is most likely not due to wave breaking at high frequencies but other high-order wave-wave interaction effects. Thus, the contradiction between the overestimation of wave crests and the underestimation of the high-frequency energy in the case of severe wave breaking implies that most breaking waves take place at low frequency and near peak frequency. This contradiction also asserts that the wave spectrum alone does not present the complete information about the wave field and the analysis of the wave crest distribution is a necessary supplement.

5 Conclusions

The manuscript presents a complete procedure for reproducing irregular sea states in a potential flow based numerical wave tank. Compared to previous research, this study furthers the advance of achieving a reproducible numerical wave tank for irregular waves by providing extensive numerical details. The comparative study of the different wave spectrum discretisation schemes and breaking wave algorithms provide insights into their impact on the statistical properties of the waves.

To summarise, a quantification of a sea state requires more than wave spectrum, the cautious check on kurtosis and wave crest distribution are crucial and necessary. The effects of the spectrum discretisation schemes and the wave breaking algorithms are sometimes seemingly less significant for one wave property but have bigger impact on the other. In order to achieve a well represented irregular sea state, the choice of numerical wave tank domain size, frequency range, horizontal grid size, vertical σ-coordinate arrangement and a time stepping are all important factors. The domain size should allow enough space for the irregular wave field to develop. The examination of the kurtosis spatial variation is a key method to ensure enough domain size and that the locations of wave gauges are far enough from the wave generation boundary. This is in contrast of a regular wave study where the wave gauges close

to the wave generation boundary are preferred. The frequency range is chosen so that all wave components fulfil the linear wave theory and that the vast majority of wave energy is represented. The horizontal grid resolution is based on the principle that the shortest wave component (highest frequency) has a required amount of cells per wavelength. The time stepping is based on the horizontal grid size and the phase velocity of the fastest wave component (lowest frequency). The vertical grid arrangement follows the constant truncation error method to ensure the correct dispersion relation. With the provided procedure, the potential flow model REEF3D::FNPF is used to reproduce distinct sea states. The computational time to real time ratio for the 3.5-hour simulations is found to be between 1.3 and 3.4. A near linear computational scalability is found up to 512 cores when at least 20000 cells per core is used. Generally, the kurtosis is stable, the computed spectra match the inputs and the wave crest distributions are within theoretical bounds. For a spectrum where most energy is concentrated near the peak frequency, such as the JMB case, the EEM method is seen to produce the spectrum shape well. When a spectrum is more evenly distributed over the frequency, such as the JNB case, the EEM method has a tendency to show higher energy concentration near the peak frequency than theory. The viscous damping algorithm is seen to be more stable in preserving the kurtosis and wave spectrum, while the filtering algorithm produces more varying results. The combined use of the PEM method and the viscous damping breaking algorithm seems to give a more universal solution considering kurtosis, spectra shape and wave crest distribution. With increasing severity of wave breaking, more energy loss is seen at the high frequency part of the spectra, and the wave crest distribution has a trend to exceed the upper limit.

In conclusion, the methodology described in the manuscript fills the gap of a guideline in the practice of numerical reproduction of irregular sea state, especially for potential flow models with σ-grid. The procedure is seen to be effective for various sea states with different wave spectra and severities of wave breaking. For future work, it is suggested to apply more adaptive breaking wave algorithms to improve the shape of wave spectra at higher frequency domain with severe breaking. The proposed procedure and criteria in the manuscript are still applicable in such investigations.

Acknowledgement

This study has been carried out as part of the E39 fjord crossing project (No. 304624) and the authors are grateful for the grants provided by the Norwegian Public Roads Administration. The computations were performed on resources provided by UNINETT Sigma2 - the National Infrastructure for High Performance Computing and Data Storage in Norway.

References

(2016). Hos-ocean: Open-source solver for nonlinear waves in open ocean based on high-order spectral method. *Computer Physics Communications*, **203**, 245 – 254. ISSN 0010-4655. 10.1016/j.apor.2021.102898https://doi.org/10.1016/j.cpc.2016.02.017.

Aggarwal, A., Chella, M.A., Bihs, H., Pákzodi, C., Berthelsen, P.A. and Arntsen, Ø.A.

(2018*a*). CFD-Based Study of Steep Irregular Waves for Extreme Wave Spectra. *International Journal of Offshore and Polar Engineering*, **28**(02), 164–170. ISSN 1053-5381.

Aggarwal, A., Pákozdi, C., Bihs, H., Myrhaug, D. and Alagan Chella, M. (2018*b*). Free surface reconstruction for phase accurate irregular wave generation. *Journal of Marine Science and Engineering*, **6**(3). ISSN 2077-1312. 10.1016/j.apor.2021.10289810.3390/jmse6030105.

Baquet, A., Kim, J. and Huang, Z. (2017). Numerical modeling using cfd and potential wave theory for three-hour nonlinear irregular wave simulations. volume Volume 1: Offshore Technology of *International Conference on Offshore Mechanics and Arctic Engineering*. 10.1016/j.apor.2021.10289810.1115/OMAE2017-61090. V001T01A002.

Bihs, H., Kamath, A., Alagan Chella, M., Aggarwal, A. and Arntsen, Ø.A. (2016). A new level set numerical wave tank with improved density interpolation for complex wave hydrodynamics. *Computers & Fluids*, **140**, 191–208.

Bihs, H., Wang, W., Pakozdi, C. and Kamath, A. (2020). REEF3D::FNPF-a flexible fully nonlinear potential flow solver. *Journal of Offshore Mechanics and Arctic Engineering*, **142**(4). ISSN 0892-7219. 10.1016/j.apor.2021.10289810.1115/1.4045915.

Bingham, H.B. and Zhang, H. (2007). On the accuracy of finite-difference solutions for nonlinear water waves. *Journal of Engineering Mathematics*. ISSN 00220833. 10.1016/j.apor.2021.10289810.1007/s10665-006-9108-4.

Bonnefoy, F., Ducrozet, G., Le Touzé, D. and Ferrant, P. (2009). *Time Domain Simulation of Nonlinear Water Waves Using Spectral Methods*, 129–164.

Bonnefoy, F., Le Touzé, D. and Ferrant, P. (2006*a*). A fully-spectral 3d time-domain model for second-order simulation of wavetank experiments. part a: Formulation, implementation and numerical properties. *Applied Ocean Research*, **28**(1), 33 – 43. ISSN 0141-1187. 10.1016/j.apor.2021.102898https://doi.org/10.1016/j.apor.2006.05.004.

Bonnefoy, F., Le Touzé, D. and Ferrant, P. (2006*b*). A fully-spectral 3d time-domain model for second-order simulation of wavetank experiments. part b: Validation, calibration versus experiments and sample applications. *Applied Ocean Research*, **28**(2), 121 – 132. ISSN 0141-1187. 10.1016/j.apor.2021.102898https://doi.org/10.1016/j.apor.2006.05.003.

CD-adapco (2016). *STAR CCM+ User Guide*. Siemens.

DNV (2011). Modelling and analysis of marine operations. Standard DNV-RP-H103, Det Norske Veritas, Veritasveien 1, Høvik, Norway.

Duarte, T., Gueydon, S., Jonkman, J. and Sarmento, A. (2014). Computation of Wave Loads under Multidirectional Sea States for Floating Offshore Wind Turbines. *Proceedings of the 33rd International conference on Ocean, Offshore and Arctic Engineering*, (June). 10.1016/j.apor.2021.10289810.1115/OMAE2014-24148.

Ducrozet, G., Bonnefoy, F., Le Touzé, D. and Ferrant, P. (2007). 3-d hos simulations of extreme waves in open seas. *Natural Hazards and Earth System Sciences*, **7**(1), 109–122. 10.1016/j.apor.2021.10289810.5194/nhess-7-109-2007.

615 Ducrozet, G., Bonnefoy, F.e.l., Le Touzé, D. and Ferrant, P. (2012). A modified High-Order
616 Spectral method for wavemaker modeling in a numerical wave tank. *European Journal of*
617 *Mechanics - B/Fluids*, **34**. 10.1016/j.apor.2021.10289810.1016/j.euromechflu.2012.01.017.

618 Engsig-Karup, A. and Bingham, H. (2009). Boundary-fitted solutions for 3d nonlinear water
619 wave-structure interaction. In: *IWWWFB24*, 20.

620 Engsig-Karup, A.P., Madsen, M.G. and Glimberg, S.L. (2012). A massively parallel gpu-
621 accelerated model for analysis of fully nonlinear free surface waves. *International Journal*
622 *for Numerical Methods in Fluids*, **70**(1).

623 FLUENT, A. (2017). *ANSYS FLUENT Tutorial Guide*. ANSYS, Inc.

624 Forristall, G.Z. (2000*a*). Wave crest distributions: Observations and second-
625 order theory. *Journal of Physical Oceanography*, **30**(8), 1931–1943.
626 10.1016/j.apor.2021.10289810.1175/1520-0485(2000)030¡1931:WCDOAS¿2.0.CO;2.

627 Forristall, G.Z. (2000*b*). Wave crest distributions: Observations and second-order theory.
628 *Journal of Physical Oceanography*, **30**(8), 1931–1943.

629 Glimberg, L.S., Engsig-Karup, A.P., Nielsen, A.S. and Dammann, B. (2013). Development of
630 software components for heterogeneous many-core architectures. In: R. Couturier (Editor),
631 *Designing Scientific Applications on GPUs*, Lecture notes in computational science and
632 engineering, 73–104. CRC Press / Taylor & Francis Group.

633 Gobbi, M.F., Kirby, J.T. and Wei, G. (2000). A fully nonlinear boussinesq model for
634 surface waves. part 2. extension to o(kh)4. *Journal of Fluid Mechanics*, **405**, 181–210.
635 10.1016/j.apor.2021.10289810.1017/S0022112099007247.

636 Grilli, S.T., Guyenne, P. and Dias, F. (2001). A fully non-linear model for three-
637 dimensional overturning waves over an arbitrary bottom. *International Journal for Nu-*
638 *merical Methods in Fluids*, **35**(7), 829–867. 10.1016/j.apor.2021.10289810.1002/1097-
639 0363(20010415)35:7¡829::AID-FLD115¿3.0.CO;2-2.

640 Grilli, S.T., Subramanya, R., Svendsen, I.A. and Veeramony, J. (1994). Shoaling of solitary
641 waves on plane beaches. *Journal Waterway Port Coastal and Ocean Enigneering*, **120**(6),
642 609–628.

643 Huang, Z.J. and Guo, Q. (2017). Semi-Empirical Crest Distributions of Long-Crest Nonlinear
644 Waves of Three-Hour Duration. In: *International Conference on Offshore Mechanics and*
645 *Arctic Engineering*, 57632, V001T01A038.

646 Huang, Z.J. and Zhang, Y. (2018). Semi-Empirical Single Realization and Ensemble Crest
647 Distributions of Long-Crest Nonlinear Waves. In: *International Conference on Offshore*
648 *Mechanics and Arctic Engineering*, 51203, V001T01A032.

649 Jacobsen, N. (2011). *A Full Hydro- and Morphodynamic Description of Breaker Bar Devel-*
650 *opment*. Ph.D. thesis.

Jeschke, A., Pedersen, G.K., Vater, S. and Behrens, J. (2017). Depth-averaged non-hydrostatic extension for shallow water equations with quadratic vertical pressure profile: equivalence to boussinesq-type equations. *International Journal for Numerical Methods in Fluids*, **84**(10), 569–583. 10.1016/j.apor.2021.10289810.1002/fld.4361.

Jiang, G.S. and Shu, C.W. (1996). Efficient implementation of weighted ENO schemes. *Journal of Computational Physics*, **126**, 202–228.

Kim, J. and Bai, K. (1999). A finite element method for two-dimensional water-wave problems. *International Journal for Numerical Methods in Fluids*, **30**(1), 105–122.

Kim, J.W., Kyoung, J.H., Ertekin, R.C. and Bai, K.J. (2006). Finite-element computation of wave-structure interaction between steep stokes waves and vertical cylinders. *Journal of Waterway, Port, Coastal, and Ocean Engineering*, **132**(5), 337–347.

Kriebel, D.L. and Dawson, T.H. (1991). Nonlinear Effects on Wave Groups in Random Seas. *Journal of Offshore Mechanics and Arctic Engineering*, **113**(2), 142–147. ISSN 0892-7219. 10.1016/j.apor.2021.10289810.1115/1.2919910.

Li, B. and Fleming, C.A. (1997). A three dimensional multigrid model for fully nonlinear water waves. *Coastal Engineering*, **30**(3), 235 – 258. ISSN 0378-3839. 10.1016/j.apor.2021.102898https://doi.org/10.1016/S0378-3839(96)00046-4.

Lynett, P. and Liu, P.L. (2004). A two-layer approach to wave modelling. *Proceedings of the Royal Society of London. Series A: Mathematical, Physical and Engineering Sciences*, **460**(2049), 2637–2669. 10.1016/j.apor.2021.10289810.1098/rspa.2004.1305.

Madsen, P.A., Bingham, H.B. and Liu, H. (2002). A new Boussinesq method for fully nonlinear waves from shallow to deep water. *Journal of Fluid Mechanics*, **462**, 1–30.

Madsen, P.A., Murray, R. and Sørensen, O.R. (1991). A new form of the Boussinesq equations with improved linear dispersion characteristics. *Coastal Engineering*, **15**, 371–388.

Madsen, P.A. and rensen, O.R.S. (1992). A new form of the boussinesq equations with improved linear dispersion characteristics. part 2. a slowly-varying bathymetry. *Coastal Engineering*, **18**(3), 183 – 204. ISSN 0378-3839. 10.1016/j.apor.2021.102898https://doi.org/10.1016/0378-3839(92)90019-Q.

Madsen, P.A. and Schäffer, H.A. (1998). Higher-order boussinesq-type equations for surface gravity waves: derivation and analysis. *Philosophical Transactions of the Royal Society of London. Series A: Mathematical, Physical and Engineering Sciences*, **356**(1749), 3123–3181. 10.1016/j.apor.2021.10289810.1098/rsta.1998.0309.

Magnussen, E.T. (2014). *Analysis of Low-Frequency Damping in Mooring Lines for Floating Production Units*. Ph.D. thesis, Norwegian University of Science and Technology, Department of Marine Technology.

Mayer, S., Garapon, A. and Sørensen, L.S. (1998). A fractional step method for unsteady free surface flow with applications to non-linear wave dynamics. *International Journal for Numerical Methods in Fluids*, **28**, 293–315.

689 Monteban, D. (2016). Numerical modelling of wave agitation in ports and access channels.

690 Nwogu, O. (1993). Alternative form of Boussinesq equations for nearshore wave propagation.
691 *Journal of Waterways, Port, Coastal, and Ocean Engineering*, **119**(6), 618–638.

692 OpenFOAM (2019). *OpenFOAM7 User Guide*. The OpenFOAM Foundation.

693 Pakozdi, C., Wang, W., Bihs, H. and Fouques, S. (2019). Validation of a high-performance
694 computing nonlinear potential theory based numerical wave tank for wave structure inter-
695 action. In: *Proceedings of the Coastal Structures Conference 2019*, 127–137.

696 Raoult, C., Benoit, M. and Yates, M.L. (2016). Validation of a fully
697 nonlinear and dispersive wave model with laboratory non-breaking ex-
698 periments. *Coastal Engineering*, **114**, 194 – 207. ISSN 0378-3839.
699 10.1016/j.apor.2021.102898https://doi.org/10.1016/j.coastaleng.2016.04.003.

700 Shu, C.W. and Osher, S. (1988). Efficient implementation of essentially non-oscillatory shock
701 capturing schemes. *Journal of Computational Physics*, **77**, 439–471.

702 Smit, P., Zijlema, M. and Stelling, G. (2013). Depth-induced wave breaking in a non-
703 hydrostatic, near-shore wave model. *Coastal Engineering*, **76**, 1–16. ISSN 0378-3839.
704 10.1016/j.apor.2021.102898https://doi.org/10.1016/j.coastaleng.2013.01.008.

705 Stelling, G.S. and Duinmeijer, S.P.A. (2003). A staggered conservative scheme for every froude
706 number in rapidly varied shallow water flows. *International Journal for Numerical Methods*
707 *in Fluids*, **43**(12), 1329–1354. 10.1016/j.apor.2021.10289810.1002/fld.537.

708 Torsethaugen, K. (1993). Two peak wave spectrum model. *Proceedings of the International*
709 *Conference on Offshore Mechanics and Arctic Engineering - OMAE*, **2**, 175–180.

710 Torsethaugen, K. (1996). Model for double peakedwave spectrum. Report SINTEF Report
711 STF22 A96204, SINTEF.

712 Torsethaugen, K. and Haver, S. (2004). Simplified Double Peak Spectral Model For Ocean
713 Waves. In: *The Fourteenth International Offshore and Polar Engineering Conference*, 9.
714 International Society of Offshore and Polar Engineers, Toulon, France.

715 van der Vorst, H. (1992). BiCGStab: A fast and smoothly converging variant of Bi-CG for
716 the solution of nonsymmetric linear systems. *SIAM Journal of Scientific Computing*, **13**,
717 631–644.

718 van Groesen, E. and Andonowati (2007). Variational derivation of kdv-type models
719 for surface water waves. *Physics Letters A*, **366**(3), 195 – 201. ISSN 0375-9601.
720 10.1016/j.apor.2021.102898https://doi.org/10.1016/j.physleta.2007.02.031.

721 van Groesen, E., Andonowati, She Liam, L. and Lakhturov, I. (2010). Ac-
722 curate modelling of uni-directional surface waves. *Journal of Computa-*
723 *tional and Applied Mathematics*, **234**(6), 1747 – 1756. ISSN 0377-0427.
724 10.1016/j.apor.2021.102898https://doi.org/10.1016/j.cam.2009.08.024. Eighth Inter-
725 national Conference on Mathematical and Numerical Aspects of Waves (Waves 2007).

Wang, W., Bihs, H., Kamath, A. and Arntsen, O.i.A. (2018*a*). Multi-directional irregular wave modelling with cfd. volume 22, 521–528. Springer.

Wang, W., Kamath, A. and Bihs, H. (2018*b*). CFD Simulations of Multi-Directional Irregular Wave Interaction With a Large Cylinder.

Wang, W., Kamath, A., Pakozdi, C. and Bihs, H. (2019). Investigation of focusing wave properties in a numerical wave tank with a fully nonlinear potential flow model. *Journal of Marine Science and Engineering*, **7**(10). ISSN 2077-1312. 10.1016/j.apor.2021.10289810.3390/jmse7100375.

Wang, W., Martin, T., Kamath, A. and Bihs, H. (2020). An improved depth-averaged non-hydrostatic shallow water model with quadratic pressure approximation. *International Journal for Numerical Methods in Fluids*. 10.1016/j.apor.2021.10289810.1002/fld.4807.

Yates, M.L. and Benoit, M. (2015). Accuracy and efficiency of two numerical methods of solving the potential flow problem for highly nonlinear and dispersive water waves. *International Journal for Numerical Methods in Fluids*, **77**(10), 616–640. 10.1016/j.apor.2021.10289810.1002/fld.3992.

Zijlema, M. and Stelling, G. (2008). Efficient computation of surf zone waves using the nonlinear shallow water equations with non-hydrostatic pressure. *Coastal Engineering*, **55**(10), 780 – 790. ISSN 0378-3839. 10.1016/j.apor.2021.102898https://doi.org/10.1016/j.coastaleng.2008.02.020.

Zijlema, M., Stelling, G. and Smit, P. (2011). Swash: An operational public domain code for simulating wave fields and rapidly varied flows in coastal waters. *Coastal Engineering*, **58**(10), 992 – 1012. ISSN 0378-3839. 10.1016/j.apor.2021.102898https://doi.org/10.1016/j.coastaleng.2011.05.015.

Zijlema, M. and Stelling, G.S. (2005). Further experiences with computing non-hydrostatic free-surface flows involving water waves. *International Journal for Numerical Methods in Fluids*, **48**(2), 169–197. 10.1016/j.apor.2021.10289810.1002/fld.821.